

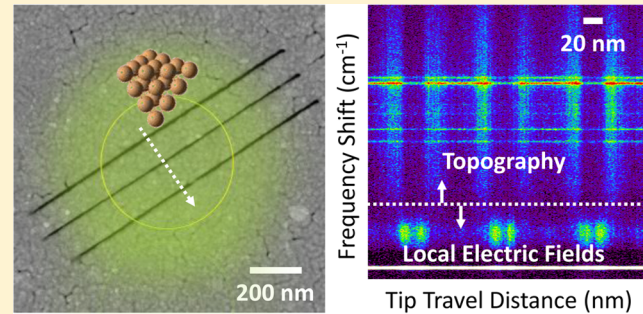
## Tip-Enhanced Raman Nanographs: Mapping Topography and Local Electric Fields

Patrick Z. El-Khoury\*,† Yu Gong,† Patricia Abellán,† Bruce W. Arey,‡ Alan G. Joly,† Dehong Hu,‡ James E. Evans,‡ Nigel D. Browning,† and Wayne P. Hess\*,†

†Physical Sciences Division and ‡Environmental and Molecular Sciences Laboratory, Pacific Northwest National Laboratory, Richland, Washington 99352, United States

### Supporting Information

**ABSTRACT:** We report tip-enhanced Raman imaging experiments in which information on sample topography and local electric fields is simultaneously obtained using an all-optical detection scheme. We demonstrate how a Raman-active 4,4'-dimercaptostilbene (DMS)-coated gold tip of an atomic force microscope can be used to simultaneously map the topography and image the electric fields localized at nanometric (20 and 5 nm wide) slits lithographically etched in silver, all using optical signals. Bimodal imaging is feasible by virtue of the frequency-resolved optical response of the functionalized metal probe. Namely, the probe position-dependent signals can be subdivided into two components. The first is a 500–2250  $\text{cm}^{-1}$  Raman-shifted signal, characteristic of the tip-bound DMS molecules. The molecules report on topography through the intensity contrast observed as the tip scans across the nanoscale features. The variation in molecular Raman activity arises from the absence/formation of a plasmonic junction between the scanning probe and patterned silver surface, which translates into dimmed/enhanced Raman signatures of DMS. Using these molecular signals, we demonstrate that sub-15 nm spatial resolution is attainable using a 30 nm DMS-coated gold tip. The second response consists of two correlated sub-500  $\text{cm}^{-1}$  signals arising from mirror-like reflections of (i) the incident laser field and (ii) the Raman scattered response of an underlying glass support (at 100–500  $\text{cm}^{-1}$ ) off the gold tip. We show that both the reflected low-wavenumber signals trace the local electric fields in the vicinity of the nanometric slits.



**KEYWORDS:** Tip-enhanced Raman, junction plasmon, nanoscale imaging, local electric fields, nanolithography

Tip-enhanced Raman spectroscopy (TERS)<sup>1–4</sup> is a rapidly evolving technique with potential applications spanning the realms of ultrasensitive chemical and biological imaging, catalysis, as well as material sciences. TERS is made possible through a unique combination of scanning probe microscopy and Raman spectroscopy. As such, it inherently possesses the spatial resolution attainable using scanning probe techniques<sup>3</sup> (e.g., atomic force microscopy, AFM) as well as the chemical selectivity and sensitivity of plasmon-enhanced Raman scattering.<sup>5</sup> The ultimate detection limit of a single molecule is attainable in TERS,<sup>6,7</sup> and it was recently demonstrated that vibrations within a single molecule<sup>8</sup> can be imaged through TERS experiments conducted under ultrahigh vacuum and ultralow temperatures. Single molecule detection sensitivity in Raman spectroscopy can be reached at plasmonic nanojunctions, where electric fields are localized and enhanced.<sup>5,6,9</sup> The possibility of ultrasensitive nanoscale chemical imaging has driven much of the interest in this field over the past decade.

In a series of recent reports from our group, we examined the information content in TER point spectra<sup>10–12</sup> and images<sup>13</sup> recorded by taking advantage of light confinement at plasmonic tip–sample junctions, all using 4,4'-dimercaptostilbene (DMS)

and a structurally related biphenyl-4,4'-dithiol system as prototypical molecular reporters. We distinguished between two regimes encountered in AFM-based TERS of the two dithiols.<sup>10</sup> In contact mode TERS experiments,<sup>11,12</sup> in which a plasmonic junction is formed between a metal AFM tip in contact with a metal surface coated with the dithiols, we identified optical signatures<sup>5</sup> of current carrying charge-transfer plasmons.<sup>14,15</sup> In noncontact mode TERS, where the AFM probe oscillates atop the dithiol-coated metal substrate, molecular orientation-dependent Raman scattering was recognizable in TER point spectra<sup>10</sup> as well as nanoscale TER images.<sup>13</sup> Overall, the interplay between molecules and plasmons is evident in TERS experiments conducted both at the classical and quantum regimes of plasmons. Nevertheless, direct access to the local electric fields in TERS (and surface-enhanced Raman spectroscopy) has proven elusive, aside from a few demonstrations.<sup>5,16</sup> Herein, we describe frequency-resolved TERS imaging experiments in which localized electric fields are imaged using an optical detection scheme.

**Received:** December 4, 2014

**Published:** March 5, 2015

The sample consists of a 20 nm thick silver film evaporated on a 10 nm thick silicon nitride membrane, see Figure 1. Tens

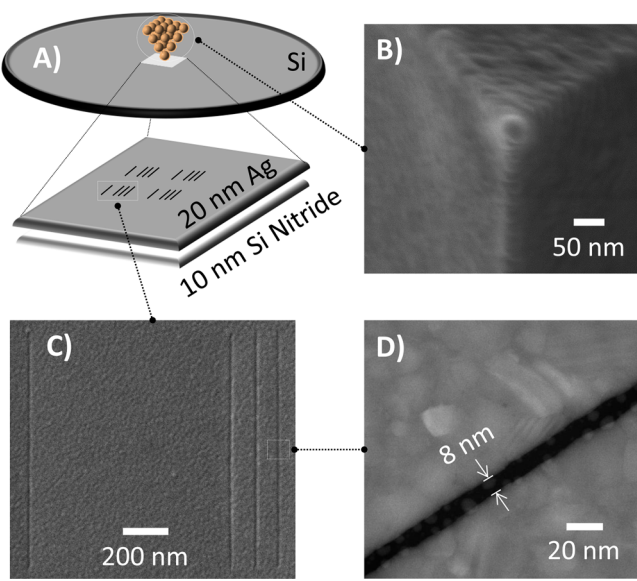


**Figure 1.** (A) Schematic illustration of the substrate, consisting of a low stress silicon nitride membrane (10 nm thick) over a  $50 \times 50 \mu\text{m}^2$  window centered on a  $200 \mu\text{m}$  thick silicon frame ( $\sim 3 \text{ mm}$  diameter). A 20 nm polycrystalline Ag film is evaporated on the substrate by arc-discharge physical laser vapor deposition. (B) HIM image of a 4,4'-dimercaptostilbene-coated Au AFM tip ( $\sim 30 \text{ nm}$  cone radius). (C) HIM image of one of the repeating patterns etched within the  $50 \times 50 \mu\text{m}^2$  window using helium ion lithography. (D) Transmission electron microscopy image revealing the morphology of a lithographically etched sub-10 nm slit (trench).

of patterns ( $3 + 1$  slits/pattern) were milled into the silver film using helium ion lithography (HIL). A representative helium ion microscopy (HIM) image of one pattern is shown in Figure 1C. A transmission electron microscopy (TEM) image of one of the nanometric trenches comprising the pattern is shown in Figure 1D, revealing that uniform sub-10 nm slits with rather sharp edges can be readily fashioned using HIL. Our general observation is that in the sub-10 nm regime, slit widths are ultimately determined by local topological features of the sputtered metal film. Namely, the local crystalline faces of nanometric structures (or grains) that make up the sputtered film are randomly oriented and exhibit different etching rates for the defined milling direction, and this dictates the slit width attainable using HIL. This is clearly evident in Supporting Information Figure S1, where the grain that causes the narrowing of the slit to a 1.3 nm gap is significantly rotated in relation to the particles on either side. The main objective of this work is to exploit the optical response of a DMS-coated gold AFM probe (30 nm cone radius) to characterize the lithographically patterned structures, see Figure 1B. We begin by describing experiments in which TER images were recorded by scanning the functionalized AFM tip over three adjacent 20 nm wide slits.

The substrate is placed on a 0.1 mm thick microscope slide. Following laser-tip alignment, the AFM probe is scanned across three 20 nm-wide slits spaced by 100 nm. The nanostructures are irradiated through the glass support from the back (silicon nitride) side of the sample using a 514 nm laser source, focused at the sample surface using a 40 $\times$  (0.7 NA) microscope

objective. Raman spectra were sequentially recorded with an integration time of 0.1 s per spectrum. Figure 2A is a contour plot representation of the recorded tip position-dependent optical response in the  $-100$  to  $2250 \text{ cm}^{-1}$  spectral range. The recorded spectra can be monitored by tracing the tip trajectory at different frequencies (Figure 3) or by taking spectral cuts at different tip positions, as shown in Figure 2B. When the tip resides toward the center of a slit, for example, at 142 nm for the central trench, the optical response in the  $500$ – $2250 \text{ cm}^{-1}$  region of the spectrum is weak when compared to its analogue that was recorded when the probe resides near the edge of the slit at 122 nm. The broad Raman response of the glass slide centered at  $\sim 300 \text{ cm}^{-1}$  as well as the laser line reflection at  $0 \text{ cm}^{-1}$  (shown in the inset of Figure 2B) are relatively suppressed when the tip is atop the silver surface and more prominent when the tip resides in the trench. To rigorously examine the correlation between the various frequencies probed, we performed a 2D correlation analysis of the raw data shown in Figure 2A. The cross-correlation between two frequencies of the recorded spectra is given by

$$\chi_{ij} = \frac{\sigma_{jk}}{\sqrt{\sigma_{jj}} \sqrt{\sigma_{kk}}}$$

where  $\sigma_{jk}$  is the covariance, and  $\sigma_{jj}$ ,  $\sigma_{kk}$  correspond to the statistical variance at frequencies  $j$  and  $k$ . The result is shown in Figure 2C and representative cross-correlation slices are plotted in Figure 2D. Cross-correlation slices taken at  $0$  and  $1580 \text{ cm}^{-1}$  reveal that (i) the  $0 \text{ cm}^{-1}$  laser signal is strongly correlated with the  $100$ – $500 \text{ cm}^{-1}$  Raman response of the glass substrate and (ii) both the aforementioned low-wavenumber signals are inversely correlated with the  $500$ – $2250 \text{ cm}^{-1}$  Raman signature of DMS molecules,<sup>12,13</sup> residing at the tip. As a strong correlation is observed between the  $0$  and  $300 \text{ cm}^{-1}$  traces, both are assigned to reflection of the laser light and Raman signal of the glass support off the tip, respectively. Because the  $0$  and  $100$ – $500 \text{ cm}^{-1}$  reflection signals of different origin are correlated, this analysis suggests that they report on the same process. More evidence for this assignment will follow. In this picture, the recorded signals are subdivided into two spectral regions: two correlated sub- $500 \text{ cm}^{-1}$  reflection signals centered at  $0$  and  $300 \text{ cm}^{-1}$  and a  $500$ – $2250 \text{ cm}^{-1}$  molecular Raman signal. When the tip resides in the trench, the reflection signals are intense and the molecular response is weak. The inverse scenario is encountered when the tip resides outside the trench atop the metal surface, where a plasmonic junction is formed between the gold tip of the AFM and the silver film. Here, the molecular response is further enhanced by the junction plasmon, and the reflection signals are dimmed because of the intervening 20 nm silver film, which effectively acts as neutral density filter ( $\text{OD} \approx 0.35$  at 514 nm). Overall, enough contrast is observed in the frequency-resolved optical response recorded in/beyond the trench, allowing us to extract valuable information about the system through the reflected and scattered signals.

In Figure 3, we monitor the tip-position-dependent optical response at different frequencies. The first two slices are taken at  $0$  and  $300 \text{ cm}^{-1}$ , see Figure 3A. Consistent with the above discussion and assignments, the two signals trace similar profiles. Both signals exhibit a twin peak structure, and trace an intensity pattern that is attenuated when the tip resides atop the silver surface, peaks in the vicinity of the edges of the three imaged slits, and is weaker when the tip resides toward the

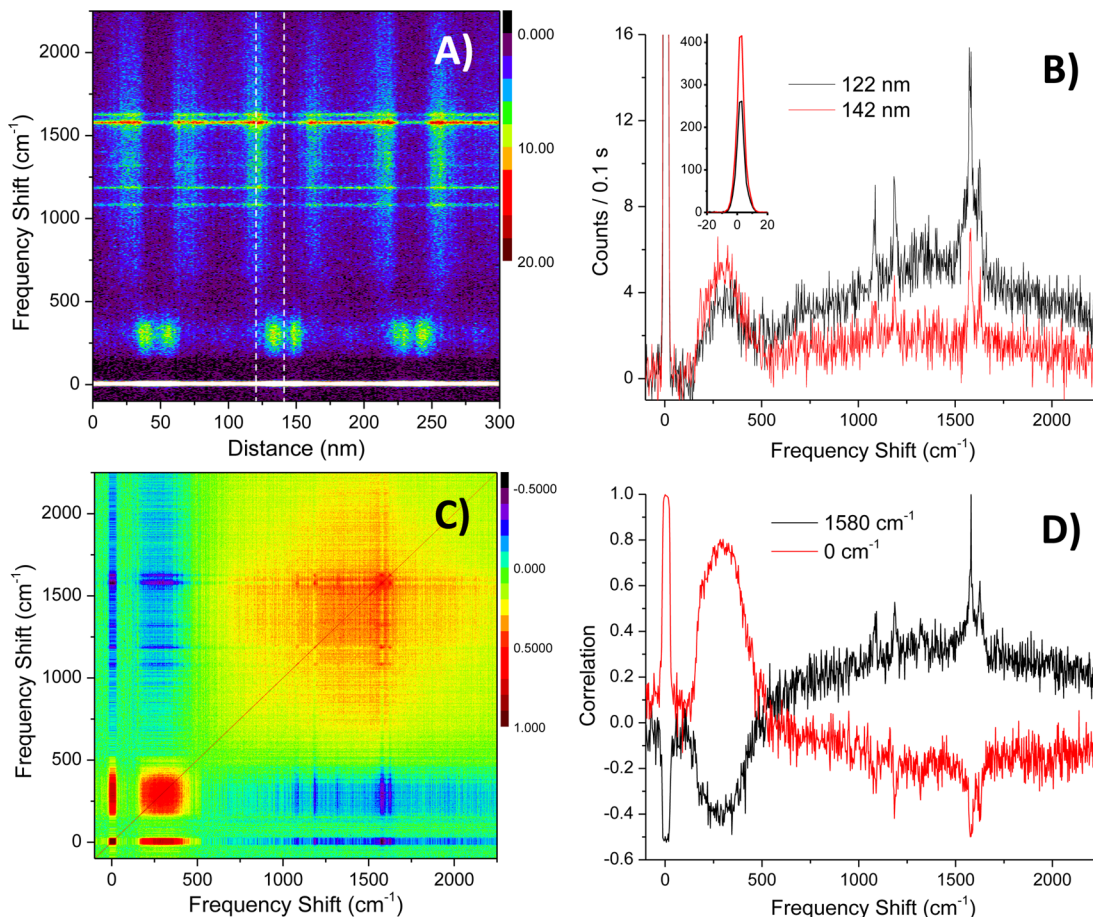


**Figure 2.** (A) Optical spectra recorded at different positions of the 4,4'-dimercaptostilbene-coated Au tip mapping three adjacent slits (~20 nm width, 100 nm center-to-center separation). (B) Spectral cuts taken at two tip positions corresponding to the edge (122 nm) and center (142 nm) of the middle slit. (C) Cross-correlation map ( $\rho_{ij} = (\sigma_{jk}^2 / \sigma_{jj} \cdot \sigma_{kk})$ ) of the data shown in Panel A). The diagonal correlation ( $\nu_j = \nu_k$ ) is 1. (D) Cross-correlation slices ( $\nu_j \neq \nu_k$ ) are taken at 0 and  $1580 \text{ cm}^{-1}$ . The reader is referred to the main text for more details.

center of the nanometric slits. Similar twin peak structures are observed in finite difference time domain (FDTD) simulations of the electric fields localized at nanometric trenches. Besides some broadening, the intensity profiles recorded at 0 and  $300 \text{ cm}^{-1}$  strongly resemble the FDTD-computed local electric fields sustained in the vicinity of nanometric trenches in silver (15 and 20 nm compared in Figure 3B). Note that the FDTD simulations assume perfect surface and slit structures. In practice, nanometric asperities sustained near the lithographically patterned slits, as well as tip convolution, are both expected to further complicate the recorded response. Nonetheless, the twin peak structure is well resolved in the TERS cross-sectional images. It appears that the light reflected off the tip traces the electric fields localized at the trenches. In other words, the tip acts as a near field reflector under the experimental conditions used herein (light polarized along the short axis of the trench in an inverted optical microscope). It is difficult to comment on (i) how the tip radius affects the recorded profiles, and (ii) the resolution attainable using the reflection signals on the basis of these results alone. Both issues will be further addressed in the ensuing section, where our resolution limits are gauged using finer slits. Conversely, Raman intensity profiles taken at  $1628$ ,  $1582$ , and  $1087 \text{ cm}^{-1}$  shifts, corresponding to vinyl  $\text{C}=\text{C}$ , aryl  $\text{C}=\text{C}$ , and  $\text{C}-\text{S}(\text{H})$  stretching vibrations of DMS,<sup>12,13</sup> paint a different picture, see Figure 3C. In this case, the recorded signals exhibit a

markedly sharp drop in intensity near the two edges of the slits, and the intensities toward the center of the trench are comparable to the signals recorded directly from the DMS-coated gold tip in the absence of the silver film. The cross sections taken using the molecular response are effectively gap-mode TERS contrast images, which provide topographic information. In the absence of a plasmonic junction that enhances the molecular response, the gold tip surface-enhanced scattering signal is weak, and it is this contrast that governs the recorded profiles. In principle, the resolution attainable using the molecular Raman signal is dictated by the extent of spatial confinement of the junction plasmon formed between the gold probe and the nanostructured polycrystalline silver surface. The cross-sectional images shown in Figure 3C clearly demonstrate that sub-20 nm resolution is attainable using a 30 nm AFM tip coated with molecular reporters. Note that both the simultaneously recorded electric field profiles (Figure 3A,B) as well as the gap-mode TERS topological cross sections (Figure 3C) consistently indicate that the widths of all three adjacent slits imaged are on the order of 20 nm.

In Figure 4, we analyze a representative image recorded by scanning a DMS-coated gold AFM tip through an isolated ~5 nm-wide slit. A contour plot representation of the data is shown in Figure 4A. A close inspection of this image reveals that the same trend is again observed: the spectral response can be subdivided into two regions that report on the local electric

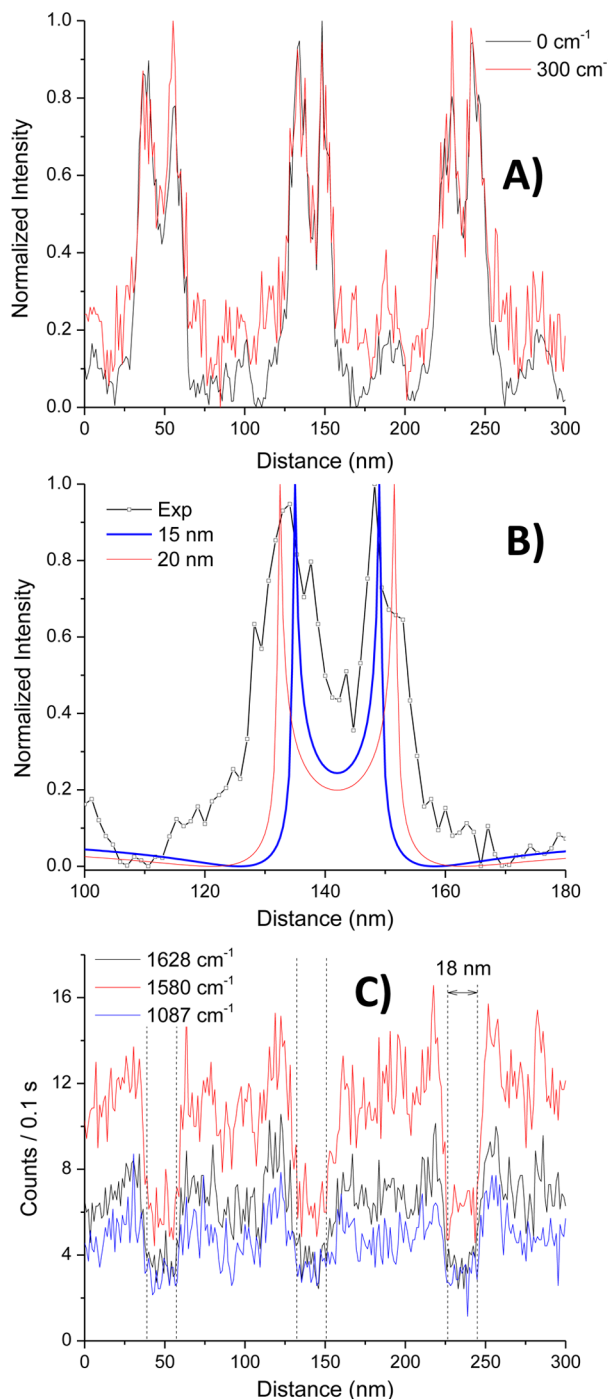


**Figure 3.** Further analysis of the spectra shown in Figure 2A. The recorded intensities at 0 and  $300\text{ cm}^{-1}$  (A) are monitored at different positions of the DMS-coated Au tip, which is scanned over three adjacent lithographically etched trenches ( $\sim 20\text{ nm}$  width,  $100\text{ nm}$  center-to-center separation). In panel B, the laser signal at  $0\text{ cm}^{-1}$  (also shown in panel A of this figure) is compared to the FDTD simulated local electric fields ( $E_{\text{total}}/E_0$ ) sustained near isolated  $15$  and  $20\text{ nm}$  wide slits following focused ( $40\times$  objective,  $0.7\text{ NA}$ )  $514\text{ nm}$  irradiation. Note that the FDTD simulations assume perfect surface and slit structures. Panel C shows the recorded intensities at  $1628$ ,  $1580$ , and  $1087\text{ cm}^{-1}$  (molecular signals) as a function of tip position.

fields through the reflected signals ( $<500\text{ cm}^{-1}$ ) and trench topography through the molecular signals ( $500\text{--}2250\text{ cm}^{-1}$ ) recorded in the absence/presence of a tip–surface plasmonic junction. This is also evident from the spectral cuts taken

toward the center of the trench and atop the silver surface, see Figure 4B. We find that in this case, the  $0$  and  $300\text{ cm}^{-1}$  slices can be uniquely fitted to a convolution of the local electric field sustained by a  $5\text{ nm}$  trench with a  $30\text{ nm}$  Gaussian profile, representative of the radius of the AFM tip used to record this image, see Figure 4C. We stress that several trench widths ( $5$ ,  $7.5$ ,  $10$ ,  $15$ , and  $20\text{ nm}$ ) as well as Gaussian widths ( $40$ ,  $35$ ,  $30$ , and  $25\text{ nm}$ ) were tested, and the best fit was obtained using the aforementioned parameters, see Supporting Information Figure S5. This result suggests that the attainable resolution in the local electric field cross-sectional images, derived from the reflection signals, is dictated by the tip radius. This is in line with our assignment of the  $0\text{ cm}^{-1}$  profiles to reflection of the laser light, as opposed to elastic or Rayleigh scattering, where much like in molecular TERS, the attainable spatial resolution should be dictated by the extent of spatial confinement of the junction plasmon. That said, we cannot completely rule out Rayleigh scattering from the nanoscopic tip based on these results alone, and this assignment will be rigorously tested in future studies. We also take advantage of electric field confinement at a plasmonic tip–sample junction in this experiment and use the Raman active vibrational modes of the tip-bound DMS molecules to obtain sub- $15\text{ nm}$  resolution through topographic gap-mode contrast TER imaging, see Figure 4D. To rigorously confirm our observations and assignments of the  $0$  and  $300\text{ cm}^{-1}$  intensity profiles to local electric field cross sections, we performed an additional control experiment in which the incident field is polarized along the long axis of a  $\sim 5\text{ nm}$  trench. In this case, the twin peak structure (convoluted with the Gaussian profile for the smaller trench) is no longer observable. Rather, the intensity profiles at  $0$  and  $300\text{ cm}^{-1}$  now trace the laser beam profile. This is consistent with the corresponding FDTD simulations, which provide further support for these assignments, see Supporting Information Figure S6. Notably, the simultaneously recorded molecular signature at  $1580\text{ cm}^{-1}$  can still be used to map the trench topography through intensity contrast in the absence/presence of a tip–surface plasmonic junction.

Several conclusions can be drawn on the basis of our observations and analysis. First, the low wavenumber signals in TERS can be used to map local electric fields. The effect seems to be reproducible and general. Much like in conventional AFM topography, the response in this case is convoluted with the tip radius. In principle, the signal-to-noise in the described measurements can be improved via plasmonic constructs which support higher TERS enhancement factors. Brighter optical signals would allow us to extract the vector components of the local electric fields at every tip position, which can be inferred from the relative intensities of the vibrational states observable through junction plasmon-enhanced Raman scattering in the single/few molecule regime.<sup>5,10,13</sup> Second, using the intensity contrast in the absence/presence of a plasmonic junction defined by the tip and patterned surface, it is possible to perform TER nanoscale chemical imaging experiments with a resolution that is finer than half the tip radius. Given the same tip, the resolution attainable in gap-mode TERS contrast imaging experiments is superior to what can be achieved using conventional AFM topography. This is because the resolution in gap-mode TERS is dictated by the extent of spatial confinement of the junction plasmon, which in turn is defined by the metal tip and metal surface. In this regard, it should be possible to further confine the plasmonic junction at the tip–sample junction and to further enhance the local electric field.

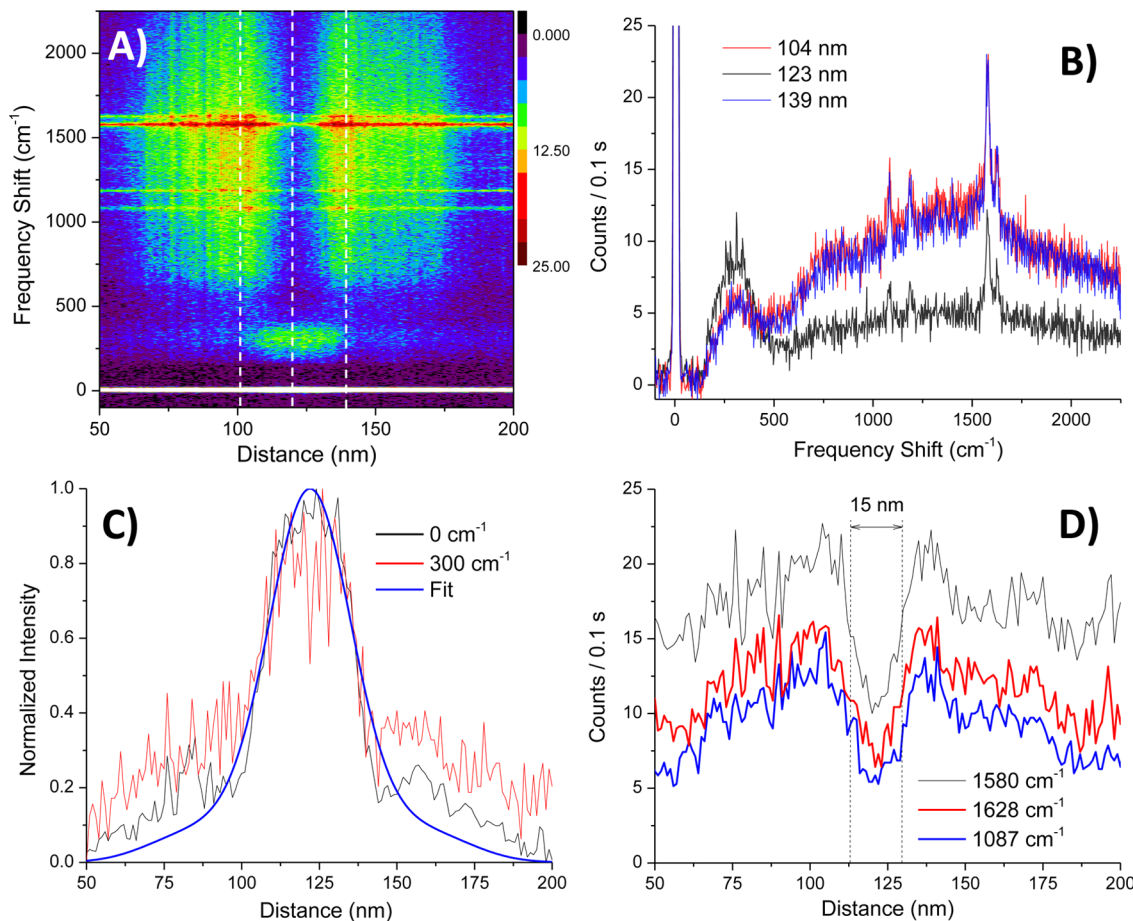


**Figure 4.** (A) Optical spectra recorded at different positions of the 4,4'-dimercaptostilbene-coated Au tip tracing an isolated slit ( $\sim 5$  nm width). (B) Spectral cuts taken at three tip positions corresponding to the center of the imaged slit (123 nm) and two positions atop the silver surface on either side of the slit (104 and 139 nm). The recorded intensities at 0 and  $300\text{ cm}^{-1}$  (C) and at  $1580$ ,  $1628$ , and  $1087\text{ cm}^{-1}$  (molecular signals, D) are monitored at different positions of the tip. Panel C also shows the convolution of a 30 nm Gaussian envelope (fwhm, representative of a 1D cross-section of the tip apex) and the FDTD simulated local electric field ( $E_{\text{total}}/E_0$ ) of a 5 nm slit. The reader is referred to the Supporting Information section for more details on the simulations and convolution procedure.

For instance, this can be accomplished using a tightly focused radially polarized laser beam,<sup>17</sup> which is expected to lead to even better spatial resolution in topological TERS contrast imaging than what is reported herein. Overall, both topographic and electric field maps can be simultaneously recorded, ensuring that the same area is probed. Moreover, equipping the scanning probe with molecular reporters renders bimodal TERS imaging experiments feasible, as defined herein, without the need for chemical functionalization of the plasmonic substrate. Third, we illustrate that it is now possible to fashion plasmonic junctions with dimensions comparable to typical molecule length scales using helium ion lithography. Advances in this regard would open way for numerous applications in the general area of plasmonic device fabrication.

**Methods.** The substrate is schematically illustrated in Figure 1. Briefly, it consists of a low stress silicon nitride membrane (10 nm thick) over a  $50 \times 50\text{ }\mu\text{m}^2$  window centered on a  $200\text{ }\mu\text{m}$  thick silicon frame ( $\sim 3$  mm diameter). A 20 nm polycrystalline Ag film is evaporated on the substrate by arc-discharge physical laser vapor deposition. The typical surface roughness measured from freshly evaporated silver films reveals a root-mean-square height distribution of  $\sim 5$  nm.

The helium ion microscope was operated at an optimal imaging voltage of 30 kV, an aperture size of  $10\text{ }\mu\text{m}$ , a spot size

of  $4\text{ }\mu\text{m}$ , and a beam blanker current of 0.5–1.5 pA. An Everhart-Thornley (E-T) detector was used to image the samples. The working distance was varied in the 5–8 mm range. Scanning transmission electron microscopy images were recorded from the same patterned regions using an 80–300 kV FEI probe Cs-corrected Titan electron microscope. All the TEM images were recorded at 300 kV.

TERS measurements were conducted under ambient conditions using an atomic force microscope (Nanoscope IIIa, Veeco Metrology) operating in noncontact mode and mounted on an inverted optical microscope (Axiovert 200, Zeiss). We employ commercial Au tips (MicroMasch) with sub-35 nm tip radii. The tips were immersed (landed) into a 1 mM solution of 4,4'-dimercaptostilbene using the AFM scanner and withdrawn after a time period of  $\sim 5$  min. The process was repeated until a detectable molecular response could be measured directly from the molecular ensemble on the tip. The incident 514 nm continuous wave laser (Innova 300, Coherent) was attenuated to  $\sim 60\text{ }\mu\text{W}/\mu\text{m}^2$  using a variable neutral density filter wheel, reflected off a dichroic beamsplitter, and focused onto the sample using an air objective (40 $\times$ , 0.7 NA). The AFM probe was aligned with the laser using noncontact TERS imaging.<sup>13</sup> The scattered signal is collected through the same objective, transmitted through a beamsplitter,

and filtered through a long pass filter. The resulting light is detected by a liquid nitrogen cooled charge coupled device coupled to a spectrometer (Holespec f/1.8i, Kaiser Optical System). The overall spectral resolution of our instrument is 8 cm<sup>-1</sup>.

## ■ ASSOCIATED CONTENT

### Supporting Information

Representative TEM and HIM images of the lithographically etched slits, FDTD simulations, simulated near field intensity profiles convolved with Gaussian profiles, additional optical images of sub-10 nm trenches, and Raman scattering from the DMS-coated gold tip. This material is available free of charge via the Internet at <http://pubs.acs.org>.

## ■ AUTHOR INFORMATION

### Corresponding Authors

\*E-mail: patrick.elkhoury@pnnl.gov.

\*E-mail: wayne.hess@pnnl.gov.

### Notes

The authors declare no competing financial interest.

## ■ ACKNOWLEDGMENTS

P.Z.E. acknowledges support from the Laboratory Directed Research and Development Program through a Linus Pauling Fellowship at Pacific Northwest National Laboratory (PNNL), an allocation of computing time from the National Science Foundation (TG-CHE130003), and the use of the Extreme Science and Engineering Discovery Environment. W.P.H. acknowledges support from the U.S. Department of Energy (DOE), Office of Science, Office of Basic Energy Sciences, Division of Chemical Sciences, Geosciences and Biosciences. The TEM work was supported by the Chemical Imaging Initiative, under the Laboratory Directed Research and Development Program at PNNL. A portion of the work was performed using EMSL, a national scientific user facility sponsored by the DOE's Office of Biological and Environmental Research and located at PNNL. This work also benefitted from PNNL Institutional Computing resources. PNNL is a multiprogram national laboratory operated for DOE by Battelle.

## ■ REFERENCES

- (1) Anderson, M. S. *Appl. Phys. Lett.* **2000**, *76*, 3130–3132.
- (2) Stockle, R. M.; Suh, Y. D.; Deckert, V.; Zenobi, R. *Chem. Phys. Lett.* **2000**, *318*, 131–136.
- (3) Pettinger, B.; Schambach, P.; Villagomez, C. J.; Scott, N. *Annu. Rev. Phys. Chem.* **2012**, *63*, 379–399.
- (4) Stadler, J.; Schmid, T.; Zenobi, R. *Nanoscale* **2012**, *4*, 1856–1870.
- (5) Banik, M.; El-Khoury, P. Z.; Nag, A.; Rodriguez-Perez, A.; Guarrotxena, N.; Bazan, G.; Apkarian, V. A. *ACS Nano* **2012**, *6*, 10343–10354.
- (6) Steidtner, J.; Pettinger, B. *Phys. Rev. Lett.* **2008**, *100*, 236101.
- (7) Sonntag, M. D.; Klingsporn, J. M.; Garibay, L. K.; Roberts, J. M.; Dieringer, J. A.; Seideman, T.; Scheidt, K. A.; Jensen, L.; Schatz, G. C.; Van Duyne, R. P. *J. Phys. Chem. C* **2012**, *116*, 478–483.
- (8) Zhang, R.; Zhang, Y.; Dong, Z. C.; Jiang, S.; Zhang, C.; Chen, L. G.; Zhang, L.; Liao, Y.; Aizpurua, J.; Luo, Y.; et al. *Nature* **2013**, *498*, 82–86.
- (9) Le Ru, E.; Etchegoin, P. G. *Annu. Rev. Phys. Chem.* **2012**, *63*, 65–67.
- (10) El-Khoury, P. Z.; Hu, D.; Hess, W. P. *J. Phys. Chem. Lett.* **2013**, *4*, 3435–3439.

- (11) El-Khoury, P. Z.; Hu, D.; Apkarian, V. A.; Hess, W. P. *Nano Lett.* **2013**, *13*, 1858–1861.
- (12) El-Khoury, P. Z.; Hess, W. P. *Nano Lett.* **2014**, *14*, 4114–4118.
- (13) El-Khoury, P. Z.; Ueltschi, T. W.; Mifflin, A. L.; Hu, D.; Hess, W. P. *J. Phys. Chem. C* **2014**, *118*, 27525–27530.
- (14) Marinica, D. C.; Kazansky, A. K.; Nordlander, P.; Aizpurua, J.; Borisov, A. G. *Nano Lett.* **2012**, *12*, 1333–1339.
- (15) Esteban, R.; Borisov, A. G.; Nordlander, P.; Aizpurua, J. *Nat. Commun.* **2012**, *3*, 825.
- (16) Marr, J. M.; Schultz, Z. D. *J. Phys. Chem. Lett.* **2013**, *4*, 3268–3272.
- (17) Novotny, L.; Hecht, B. *Principles of Nano-Optics*, 1st ed.; Cambridge University Press: New York, 2011.